FLOW CAMBRIDGE UNIVERSITY PRESS

RESEARCH ARTICLE

A computational fluid dynamics study of flame gas sampling in horizontal dilution tubes

Hartmut Mätzing[1],* , Petros Vlavakis[2], Dimosthenis Trimis[2] and Dieter Stapf[1]

[1] Karlsruhe Institute of Technology (KIT), Institute for Technical Chemistry (ITC), Hermann-von-Helmholtz-Platz 1, 76344 Eggenstein-Leopoldshafen, Germany
[2] Karlsruhe Institute of Technology (KIT), Engler-Bunte-Institute (EBI-VBT), Engler-Bunte-Ring 1, 76131 Karlsruhe, Germany
*Corresponding author. E-mail: hartmut.maetzing@kit.edu

Abstract
The performance of horizontal dilution tubes is investigated by Reynolds-averaged Navier–Stokes and large-eddy simulations. The flame gas enters the dilution tube through a pinhole. The orifice flow and the dilution process inside the tube are studied. The volume flow through the orifice is shown to be proportional to the square root of the pressure drop. The discharge coefficient is 0.9 ± 0.3 in the cold air (calibration) case and drops to 0.35 under hot (flame) conditions. The resulting dilution ratio is roughly a factor of five below typical literature data. The gas sample remains in the wall boundary layer and the mixing process is not complete at the end of the dilution tube. Turbulence decays rapidly behind the tube inlet, which shifts the flow into the laminar to turbulent transition regime. Turbulence increases significantly in the outlet section which has much smaller pipe cross-sections. Despite its relatively low Reynolds number, the outlet flow to the particle sizer (or to the gas analyzer) is clearly turbulent, and interactions with the wall are probable. The results are in agreement with previous findings from laminar jets in cross-flow. Guidelines for optimization of the sampling conditions are suggested.

Impact Statement
The paper addresses an ongoing discussion in the field of combustion diagnostics, and in the field of soot formation in particular. Since approximately 20 years ago, it has been common to use macroscopic dilution tubes for the sampling of flame gas and particulates. However, the correct functioning of the sampling procedure has not been proved so far. Here, computational fluid dynamics (Reynolds-averaged Navier–Stokes and large-eddy simulations) is used to investigate the important claims of the procedure: rapid mixing and quenching of the flame gas sample. As result, a large potential for optimization of the experimental procedure is identified. It is the first model study which considers the gas flow in the interior of the dilution tubes.

1. Introduction

Fuel rich hydrocarbon flames can give rise to soot formation, a highly complex process which involves homogeneous gas phase reactions, a gas-particle transition, heterogeneous surface growth and aerosol dynamics at high temperatures. The amount of soot which is actually formed depends on a variety of parameters such as type of fuel, fuel-to-air ratio, temperature and pressure. In the early stages of soot

CrossMark

formation, particle number densities can exceed 10^{12} cm^{-3} and particle sizes are just a few nanometres. Accurate measurements are still a challenge under such conditions. Much of the early data on soot formation were obtained from non-intrusive optical measurements of the particulate phase and from molecular beam sampling and mass spectroscopy of gas phase components. As prominent result, it was found that soot particle inception contributes only a little (roughly 10 %–20 %) to the total soot volume or mass being formed and most of the soot is formed by heterogeneous surface growth, as reviewed earlier (Haynes & Wagner, 1981; Wagner, 1979). Polycyclic aromatics were expected to be precursors of the first, nascent soot particles and finally, pyrene was identified as key intermediate in soot formation and used in the so-called HACA mechanism (hydrogen abstraction, C_2H_2 addition) to model soot formation numerically (Appel, Bockhorn, & Frenklach, 2000). The recent research focuses on the feasibility to include further polyaromatic hydrocarbons in the processes of particle inception and surface growth and on the explanation, how spherical structures can emerge from the interaction of planar precursors (Frenklach & Mebel, 2020; Johansson, Head-Gordon, Schrader, Wilson, & Michelsen, 2018; Wang, 2011).

The use of horizontal dilution tubes and scanning mobility particle sizers (SMPS) for soot particle characterization was first proposed by Kasper, Siegmann, & Sattler (1997). Later, Zhao, Yang, Johnston, et al. (2003) and Zhao, Yang, Wang, et al. (2003) extended the earlier work emphasizing the need for high dilution ratios (DR), because the upper limit of particle number concentrations is of the order 10^6–10^7 cm^{-3} in SMPS. In addition, reliable particle sampling from a high-temperature reacting environment, like postflame gases, requires fast quenching in order to suppress particle inception, surface growth and coagulation in the measurement device. A turbulent mixing process was expected to meet these requirements. Hence, it was proposed to introduce a sampling tube of approximately 10 mm diameter into the flame, feed it with a turbulent cold inert dilution gas flow and sample the hot flame gas through a small (0.1–0.5 mm inner diameter) orifice under laminar flow conditions. As an alternative to free-standing sampling tubes, these may also be embedded in cooled stagnation plates (Camacho et al., 2015). The flow arrangement corresponds to a jet in cross-flow configuration. At constant dilution gas flow, the DR is a function of the orifice diameter and the pressure drop at the orifice: DR is high for small orifice diameters and for small pressure drops. Experimentally, it was found that the measured particle size distribution changes with increasing DR and finally becomes independent of DR above some critical value which is of the order of 10^4 (Zhao, Yang, Johnston, et al., 2003; Zhao, Yang, Wang, et al., 2003). In a more recent study, the optimum DR was found to be much lower, in the range 250–1000 (Camacho et al., 2015; Tang, Mei, & You, 2016). Meanwhile, horizontal dilution tubes have also been used in the analysis of gas phase soot precursors (Adamson, Skeen, Ahmed, & Hansen, 2018).

Since the presence of a large sampling nozzle or a stagnation plate causes distortions of the flow and temperature fields in the flame, error analyses were performed by several authors both in molecular beam sampling and in conventional sampling studies to quantify these effects (Camacho et al., 2015; Egolfopoulos et al., 2014; Gururajan, Egolfopoulos, & Kohse-Höinghaus, 2015; Hansen, Cool, Westmoreland, & Kohse-Höinghaus, 2009; Saggese et al., 2016; Skovorodko, Tereshchenko, Korobeinichev, Knyazkov, & Shmakov, 2013; Struckmeier, Oßwald, Kasper, et al., 2009; Tang et al., 2016). Based on studies of the gas flow around the probe, there seems to be consensus that a horizontal dilution tube can map the flame conditions a few millimetres upstream of the sampling position correctly and no other serious errors need to be considered. Subsequent to the work by Zhao, Yang, Johnston, et al. (2003) and Zhao, Yang, Wang, et al. (2003) the described experimental set-up has been used in numerous subsequent studies, only a relevant selection of which is mentioned here (Abid et al., 2008; Camacho et al., 2015; Commodo et al., 2013, 2015; Ghiassi, Jaramillo, Toth, & Lighty, 2016; Sgro et al., 2009; Tang et al., 2016). All of these studies confirmed that fuel-rich flames of aliphatic hydrocarbons, ethylene in particular, have a great potential to develop bimodal soot particle size distributions.

As described above, previous studies have considered flow conditions and errors which may occur in the flame environment around the sampling tube. The present study is motivated by the lack of knowledge concerning the flow conditions inside the sampling tube which determine the mixing efficiency of the hot flame gas sample into the cold dilution gas flow as well as the time scales at which mixing and quenching

occur. A preliminary computational fluid dynamics (CFD) analysis showed that the mixing process is poor and is not complete when the gas enters the differential mobility analyzer (DMA) for particle size analysis (Mätzing & Stapf, 2019). The previous study is now extended to clarify the flow conditions in free-standing and in embedded horizontal dilution tubes using both Reynolds-averaged Navier–Stokes (RANS) and large-eddy simulations (LES) on grids with high spatial resolution. In addition, a revised procedure is proposed to determine the orifice flow rate and the DR.

2. Theory

The sampled gas flow is roughly 3–4 orders of magnitudes smaller than the dilution flow. Since it is not practical to measure it directly, the orifice flow is calibrated with ambient air and extrapolated to flame conditions. For the extrapolation, it is usually assumed that the orifice flow is a laminar Poiseuille flow with a flow rate proportional to the pressure drop and inversely proportional to the gas viscosity (Camacho et al., 2015; Tang et al., 2016; Zhao, Yang, Wang, et al., 2003). However, Poiseuille flow requires long pipes to develop fully with pipe length much larger than pipe diameter (Lafferty, 1998). In typical horizontal soot sampling tubes, the orifice length is given by the tube wall thickness, roughly around 0.5 mm, and hence less than five times the orifice diameter. Therefore, the orifice flow might be described better by a different approach. In this paper, the orifice flow is described by Bernoulli's equation and the dilution process is described by a jet in cross-flow concept.

2.1. Orifice flow revisited

For incompressible fluid flow (at Mach number <0.3), the orifice flow Q_{orf} is commonly described in terms of the isentropic flow rate derived from Bernoulli's equation,

$$Q_{orf} = C_d \times A_{orf} \times \sqrt{2\Delta P_{orf}/\rho},$$

(1)

where ρ is the fluid density, A_{orf} is the orifice cross-section and C_d is the discharge coefficient, which is around 0.7 typically (Borutzky, Barnard, & Thoma, 2002; Lafferty, 1998; Oertel, Prandtl, & Böhle, 2008), but may exceed 1 due to the presence of a cross-flow (Berger, Gourdain, Bauerheim, & Devillez, 2019). Isentropic flow occurs under adiabatic conditions and, for pressure drops $\Delta P_{orf} < 200$ Pa, the adiabatic cooling is expected to be less than 5 K (for diatomic gas) in horizontal flame gas sampling tubes under atmospheric conditions. Accordingly, ρ changes by less than 0.2 % and can be regarded as constant. Equation (1) predicts the orifice flow to be proportional to the square root of the pressure drop and to be independent of the gas viscosity. However, despite the vast number of publications about orifice flow, to the authors' knowledge a high-temperature validation ($T > 700$ K) of (1) is not available in the literature.

2.2. The jet in cross-flow approach

From the fluid mechanics point of view, the flame gas sampling by horizontal dilution tubes represents a jet in cross-flow arrangement, wherein the gas sample flow is the laminar jet and the cold dilution gas flow is the transverse flow. Due to their wide range of practical applications, jets in cross-flow have been investigated intensively for many years (Chang, Shao, Hu, & Zhang, 2016; Mahesh, 2013; Muppidi & Mahesh, 2005). The flow characteristics are described by several characteristic numbers:

- the jet to cross-flow velocity ratio $R = (\rho_j/\rho_\infty)^{0.5} \times u_j/u_\infty$;
- the jet to cross-flow density ratio $S = \rho_j/\rho_\infty$;
- the jet to cross-flow momentum flux ratio $J = R^2$;
- the jet Reynolds number $Re_j = u_j D_j/\mu_j, \mu_j = \eta_j/\rho_j$;

where u is velocity, ρ is density, η is dynamic viscosity, μ is kinematic viscosity, D is diameter and the subscripts are j for the jet and ∞ for the cross-flow. Different from flame gas sampling, experimental investigations usually employ long jet pipes to ensure fully developed flow. High R, J and Re_j were found to favour the mixing of the jet into the cross-flow, but even in case of laminar jets (low Re_j and R), turbulent vortex structures can develop which induce a high mixing efficiency. Yet, extremely small jet-to-cross-flow momentum flux ratios, $J < 5$, may prevent the jet from penetrating deeply into the cross-flow and may cause the jet to adhere to the wall or wall boundary layer (Karagozian, 2014; Mahesh, 2013). As shown earlier (Mätzing & Stapf, 2019), such a situation may arise under flame gas sampling conditions, when a high-temperature and high-viscosity jet enters into a much colder cross-flow with $R = 0.14$–0.77 and $J = 0.02$–0.6 (these values hold in the present study, too).

3. Computational methods

3.1. CFD simulations

The simulations were performed for free-standing and embedded dilution tubes, as outlined in figure 1(a,b). The free-standing dilution tube served as a base case. The experimental set-up was used in our laboratory previously (Frenzel, Krause, & Trimis, 2017) and it is very similar to other common set-ups (Zhao, Yang, Johnston, et al., 2003). The uncooled, free-standing ceramic (Al_2O_3) dilution tube was 9 mm inner diameter, with a wall thickness of 0.5 mm; the pinhole diameter was $D_{orf} = 0.3$ mm. The input nitrogen dilution flow was 30 s.l.p.m. (1 s.l.p.m. = 1.66×10^{-5} Nm^3 sec^{-1}), which corresponds to a Reynolds number $Re = 5000$. At the measurement locations $\Delta P1$ and $\Delta P2$ in figure 1(c), low differential pressure sensors were installed and the pressure was assumed to drop linearly along the tube axis. This assumption was confirmed during the simulations. Note that in this set-up, the outlets to the measurement device (DMA) and to the pump are in parallel, at slightly different vertical positions. Other set-ups may have different arrangements, e.g. outlets at equal vertical positions and also outlets which are oriented perpendicular to each other. Such a configuration was simulated earlier (Mätzing & Stapf, 2019) with no difference in major findings about the flow properties. Hence, the current results are taken to be valid for most of the common geometric configurations and tube materials.

The solid tube wall is not modelled explicitly; therefore the orifice is represented by a small tube which is 0.5 mm long, i.e. the wall thickness. Occasional clogging of the orifice can pose experimental problems, as will be discussed below, but it is not the object of this study.

To simulate embedded dilution tubes, the same geometric configuration is used, but the wall temperature is set to a constant appropriate value, e.g. 400 K, which results from the intense cooling by the stagnation plate (Saggese et al., 2016).

The simulations were performed for a single phase gas flow. Under sooting conditions, in particular, when the soot forming (inception) zone is studied, the soot volume fraction is typically below 10^{-7} and, the particle size is well below 100 nm, often below 10 nm. Thermophoretical effects can eventually accelerate the particle motion relative to the gas in the cooling region in front of the orifice (Saggese et al., 2016). In and behind the orifice, the nanoparticle trajectories can be expected to follow the gas flow and, particle–flow interactions are negligible due to the very small volume fraction (Corson, Mulholland, & Zachariah, 2018; Friedlander, 2000). Hence, as first approximation, two-phase flow modelling is not really mandatory to capture the important flow properties and processes in the dilution tube.

The CFD simulation was performed in three dimensions using Ansys Fluent. Two grids of different cell number and cell geometry were generated:

 (i) an unstructured grid with 18.5×10^6 tetrahedral cells, using Fluent 17.2 for RANS and LES;
(ii) an unstructured grid with 3.2×10^6 polyhedral cells, using Fluent 14.5 for RANS only.

The calculations were started with a precursor RANS calculation on grid (ii), in order to estimate the integral length scale $l_0 = k^{0.5}/(C_\mu \, \omega)$, wherein k is the turbulent kinetic energy, ω is the specific dissipation rate and $C_\mu = 0.09$ (Gerasimov, 2016). Since approximately 5–10 cells across l_0 ($\sim 270 \, \mu m$)
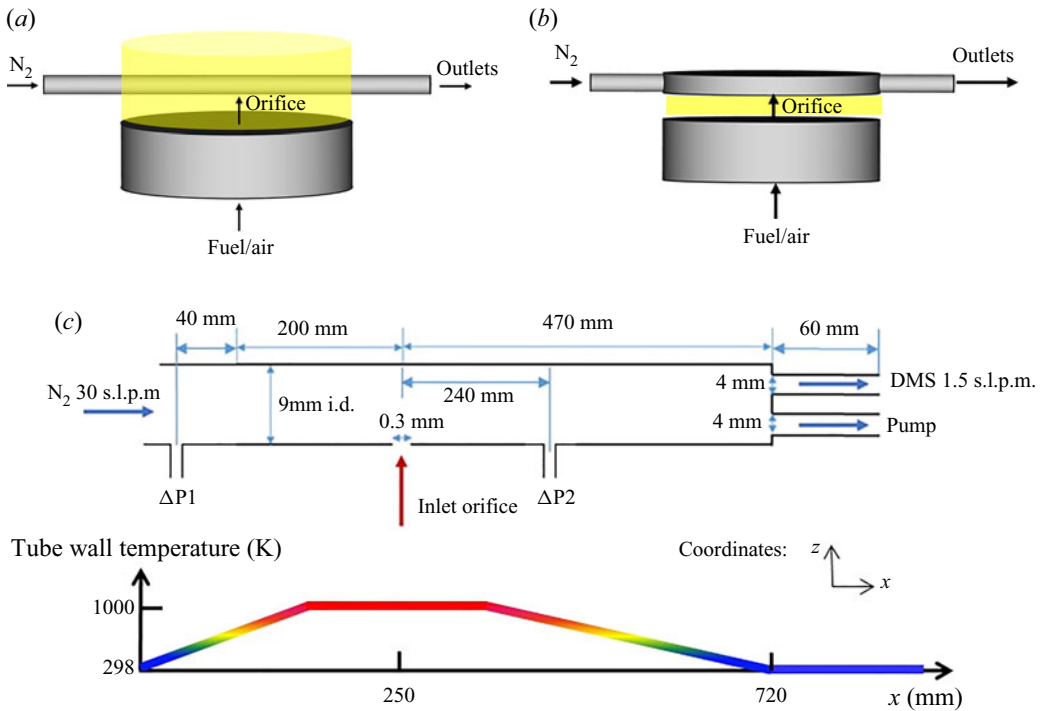
Figure 1. *Sketches of free-standing (a) and embedded (b) dilution tubes used in flame studies. Geometry of the free-standing dilution tube and wall boundary conditions (c). Tube wall temperature is 298 K under cold (calibration) conditions and 400 K for embedded tubes. For free-standing tubes, under hot (flame) conditions, the tube wall temperature profile is indicated above. Initial turbulence intensity of 5 % at N_2 inlet (see § 4.1).*

are required to resolve ∼80 % of the turbulent energy spectrum, grid (i) was generated for the LES calculations with roughly six times smaller cell volume. The two grids were also used for a study of grid independence.

The general form of the conservation equations, which are solved in CFD calculations, is

$$\frac{\partial \rho}{\partial t} + \boldsymbol{\nabla} \cdot (\rho \boldsymbol{u}) = S_m \quad \text{mass conservation or continuity,} \tag{2}$$

$$\frac{\partial}{\partial t}(\rho \boldsymbol{u}) + \boldsymbol{\nabla} \cdot (\rho \boldsymbol{u} \boldsymbol{u}) = -\boldsymbol{\nabla} P + \boldsymbol{\nabla} \cdot (\bar{\bar{\tau}}) + \boldsymbol{F_b} \quad \text{momentum,} \tag{3}$$

$$\rho \frac{\mathrm{D}E}{\mathrm{D}t} = -\boldsymbol{\nabla}(P\boldsymbol{u}) + \boldsymbol{\nabla} \cdot (\boldsymbol{u}\bar{\bar{\tau}}) + \boldsymbol{\nabla} \cdot (\lambda_G \boldsymbol{\nabla} T) + S_E \quad \text{energy,} \tag{4}$$

$$\frac{\partial \rho y_i}{\partial t} + \boldsymbol{\nabla} \cdot (\rho \boldsymbol{u} y_i + \boldsymbol{J_i}) = R_i \quad \text{species transport,} \tag{5}$$

wherein t (s) is time, P (Pa) is pressure, τ (Pa) is stress tensor, E (J) is energy, λ_G (W (m K)$^{-1}$) is heat conductivity of the gas, T (K) is temperature, y_i (−) is the mass fraction of species i, J_i (kg (m^2 s)$^{-1}$) is the diffusion flux of species i and R_i (kg (m^3 s)$^{-1}$) is a source term of species i. The source term for the mass, S_m, is zero if no condensation or evaporation processes are considered. Similarly, R_i may be zero in the absence of chemical reactions. Here F_b is the source term for momentum which can be chosen to include gravity. The source term for energy, S_E, includes heat transfer processes as well as reaction heats and heat exchange due to phase transitions, if applicable.

In the RANS calculations, the turbulence model SST k–ω was used with corrections for curvature and low Reynolds numbers Re. Near wall treatment was done by high resolution inflation layers. The spatial resolution at the walls was better than 170 µm in mesh (ii) and better than 30 µm in mesh (i). The dimensionless wall distance y^+ was always less than unity in the laminar sublayer for both meshes which means that transport properties at the wall boundary layer were fully captured (Zirwes et al., 2021).

The pressure based solver was used to solve the equation system with the SIMPLE algorithm for pressure–velocity coupling which is acceptable for transient calculations, too, according to the Ansys Fluent User's Guide. Second-order upwind schemes were used for discretization. For good convergence, the calculations were often continued until residuals dropped below 10^{-7}.

The LES calculations were performed using mesh (i) according to the ANSYS guidelines (Gerasimov, 2016). The spatial resolution was better than one fifth of the turbulence length scale which allows us to resolve roughly 80 % of the turbulent kinetic energy. For subgrid-scale modelling, the dynamic Smagorinsky model was used with wall Prandtl number set to 0.85. The time step was set to 15 µs, i.e. the average travel time across a cell.

During post-processing, the Q criterion, the λ_2 criterion as well as pressure and velocity fluctuations were used to detect vortices. In brief, the Q criterion defines a vortex in a region where the square of vorticity is larger than the square of strain rate meaning that rotational deformation is larger than stretching deformation. The λ_2 criterion determines vortex regions from the eigenvalues of the symmetric and antisymmetric parts of the velocity tensor: if two of the eigenvalues are negative, a local pressure minimum exists which induces vortex formation. None of these methods is unique for vortex identification, as has been discussed and reviewed by several authors (Fröhlich, 2006; Holmén, 2012; Jiang, Machiraju, & Thomson, 2005; Kolár, 2011). For example the Q criterion may not distinguish between shear and rotation induced vortices, the λ_2 criterion may not resolve closely neighboured vortices and some authors recommend scalar fluctuation monitoring to avoid problems related to numerical noise. But, as will be shown later, the methods used here gave very similar results showing little vortex formation in the dilution tube except close to and in the outlet pipes.

The mass or mole fractions of CO_2 were used to monitor and assess the mixing of the flame gas into the dilution gas.

3.2. *Gas properties and flow rate evaluation*

The calculations were performed for the following cold and hot conditions:

(i) ambient air conditions to simulate the experimental calibration procedure; air was taken to be dry and free of trace gases (mole fractions $x_{O_2} = 0.21$, $x_{N_2} = 0.79$);

(ii) flame conditions were simulated without the flame gas flowing around the dilution tube, just by defining the temperature to be 1000 K at the orifice (Zhao, Yang, Wang, et al., 2003) and using the tube wall temperature profile shown in figure 1, assuming a CH_4/O_2 oxy-fuel flame, equivalence ratio $\Phi = 2.4$, $C/O = 0.6$, the flame gas concentrations were estimated from Köhler et al. (2016) and from Stelzner, Weis, Habisreuther, Zarzalis, & Trimis (2017). They are listed in table 1. The selected gas mixture has a relatively high viscosity η, $\eta_{flame, 1000\,K} = 3.64 \times 10^{-5}$ kg (m s)$^{-1}$ = 364 µP, approximately 10 % higher than in usual fuel–air flames (see table 2). Its molar weight and density are half that of air.

The orifice volume flows Q_{orf} (s.l.p.m.) were determined from the calculated mass flows $\dot{m}$ (kg s^{-1}) and densities ρ (kg m^{-3}) in the following way:

$$Q_{orf}(\text{s.l.p.m.}) = \frac{\dot{m}(\text{kg sec}^{-1})}{\rho(\text{kg m}^{-3})} \times 1000(1\ \text{m}^{-3}) \times 60(\text{sec min}^{-1}) \times \frac{273.15\ \text{K}}{T_{orf}(\text{K})} \times \frac{P_{orf}(\text{Pa})}{101\,325\ \text{Pa}}, \quad (6)$$

where Q_{orf}, T_{orf} and P_{orf} all refer to the inlet ('flame side') conditions at the orifice entrance. The DR was determined from the dilution gas flow $Q_{N2, 273.15K}$ and Q_{orf} according to (7), and also from the

Table 1. *Flame gas composition, x = mole fraction.*

Gas	CO_2	CO	H_2	H_2O	C_2H_2	CH_4	C_2H_4
x (−)	0.042	0.21	0.42	0.268	0.03	0.02	0.01

Table 2. *Gas viscosities η of air and flame gas between 298 K and 1000 K.*

	Air ($x_{O_2} = 0.21$, $x_{N_2} = 0.79$)			Flame gas (see table 1)		
T (K)	298	400	1000	298	400	1000
η (µP)	186	230	429	137	174	364
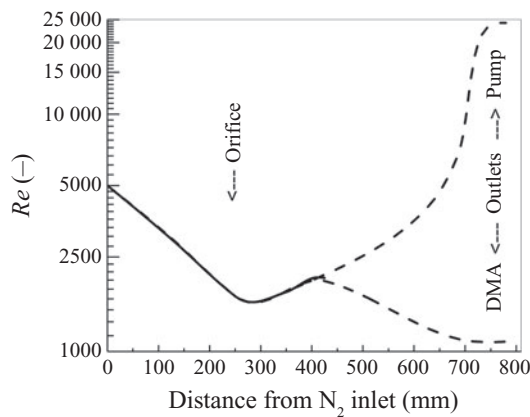
Figure 2. *Sketch of Reynolds number and flow splitting along the tube axis under hot (flame) conditions, instantaneous LES results at t = 2.25 ms.*

calculated mole fractions of CO_2 at the orifice entrance and at the DMA outlet. Equation (7) reads

$$DR = 1 + \frac{Q_{N_2, 273.15\ K}\ \text{(s.l.p.m.)}}{Q_{orf}\ \text{(s.l.p.m.)}}. \tag{7}$$

4. Results

4.1. General flow properties

In the entrance section of the dilution tube, the dilution gas flow was found to rapidly loose its initial turbulence properties. While entering the tube with an initial Reynolds number $Re \approx 5000$ and an initial turbulence intensity of 5 %, the specific turbulent dissipation rate in the dilution tube is around $\omega \approx 4000$ Hz which translates to a relaxation time $\tau_\omega \approx 250$ µs and to a relaxation length scale $l_\omega \approx 4$ mm. This behaviour is observed under hot (flame) conditions preferentially, it is much less under cold (calibration) conditions (not shown in figure 2).

Hence, Re decreases rapidly along the tube axis due to a temperature effect and falls below 2000 at the location of the orifice, as shown in figure 2. Farther downstream, Re increases a little again, and thereafter it separates into a low Re part and a high Re part. The two partial flows leave the dilution tube via the measurement (DMA) outlet and via the pump outlet, respectively (figure 2).

Figure 3 shows a contour plot of the specific dissipation rate around the orifice until approximately 200 mm downstream. It varies only between 3500 and 4500 s⁻¹ which indicates rather uniform flow
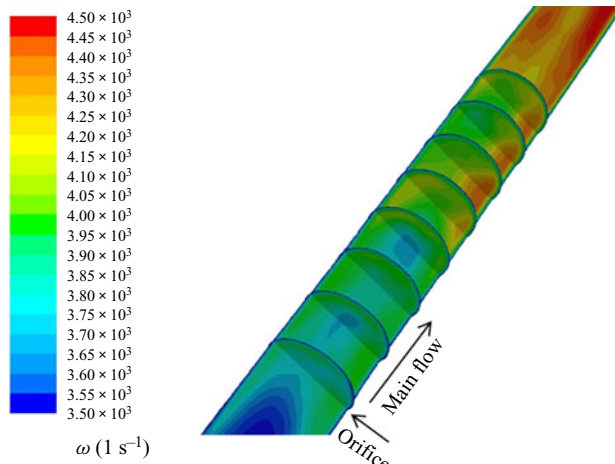
Figure 3. *Specific dissipation rate up to approximately 200 mm downstream of the orifice on central plane and on some planes perpendicular to the main flow under hot (flame) conditions, LES, instantaneous at* $t = 2.25\,ms$.
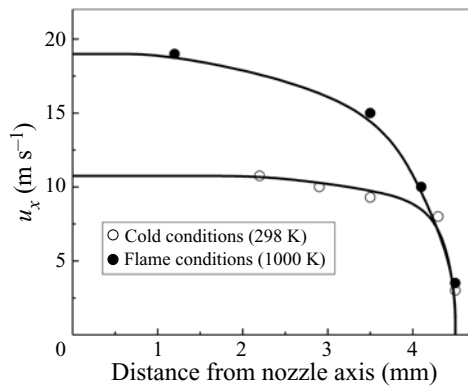

Figure 4. *Radial velocity profile (thick lines) under cold and under flame conditions in the dilution tube at the orifice location (RANS results).*

conditions. Figure 4 shows the radial velocity profile at the location of the orifice. While under cold conditions, the radial profile is rather flat, indicating turbulence, it is neither flat nor parabolic under hot (flame) conditions, which indicates the gas flow to be in the laminar to turbulent transition regime.

The results in figures 2–4 were derived from LES and RANS calculations, as indicated in the figure captions. Since RANS calculations cannot resolve details of transitional and turbulent flows, their feasibility and validity need to be investigated. As example, figure 5(*a*,*b*) compare the contour lines of the major flow velocity u_x in the vicinity of the orifice inlet as obtained from RANS and LES calculations. Both results are very similar, e.g. the area weighted average u_x is 13.5 m s^{-1} in both cases. This confirms the feasibility of RANS calculations in the present model. Moreover, RANS results obtained from both meshes (i) and (ii) also agree quite well which confirms the grid independence of results for these high resolution meshes.

4.2. Detection of vortex structures

Vorticity is a measure of the local spin rate and hence a good indicator for the presence and intensity of vortices. In the vicinity of the orifice, the vorticity ranges from $\omega_v = 5 \times 10^2$–2×10^4 s^{-1} and, if plotted
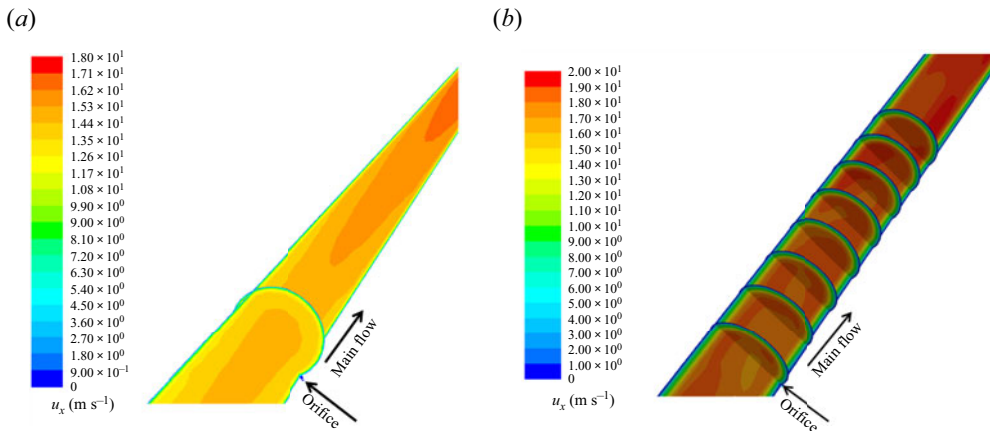
(a)

(b)

Figure 5. (a) Here, RANS – contours of x-velocity u_x under hot (flame) conditions (using mesh (ii)) in the tube central plane from orifice location up to 200 mm downwards, a plane perpendicular to the main flow is shown also. (b) Here,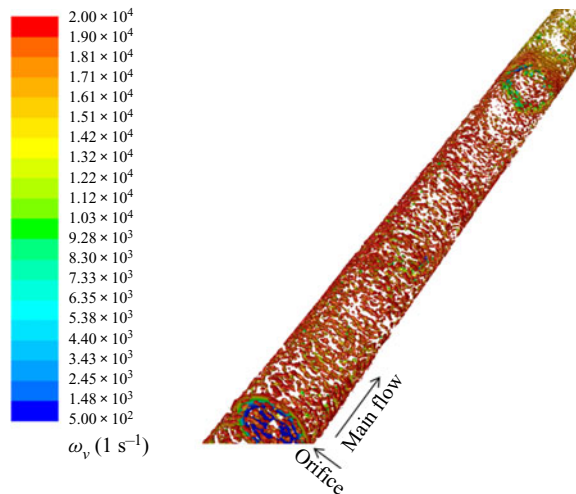 LES – contours of x-velocity u_x (instantaneous at $t = 2.25$ ms under hot (flame) conditions), obtained with mesh (i), in the tube central plane from orifice location up to 200 mm downwards, some planes perpendicular to the main flow are shown also.

Figure 6. Isosurface $\lambda_2 = -8 \times 10^4$ coloured by vorticity from orifice location up to 200 mm downwards (instantaneous at $t = 2.25$ ms under hot (flame) conditions).

on isosurfaces of the Q or λ_2 criteria, low vorticity values are found around the tube axis, while high vorticity values prevail close to the wall, as shown in figure 6.

The observable vortex structures are tiny and quite uniformly distributed which indicates rather homogeneous flow conditions. This changes significantly towards the outlet section, where the vorticity reaches values above 10^5 s^{-1} and large vortex structures are visible (figure 7). Large vortex structures develop in the pump outlet, but it is remarkable that large scale structures are also visible in the DMA outlet despite its low *Re* number. Obviously, the length of the outlet tube is too short to level out the turbulent motion which originates from the region where the flow splitting starts. This is illustrated further in figure 8 which compares the pathlines in the two outlets. While the trajectories are parallel in the pump outlet, they are twisted or meandering in the DMA outlet. Turbulent flow at low Reynolds
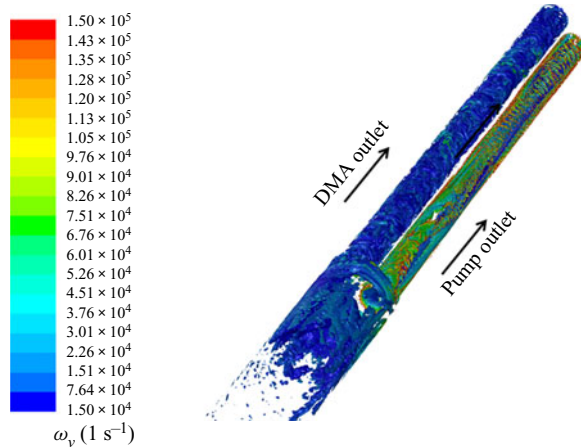
Figure 7. *Isosurface $\lambda_2 = -8 \times 10^4$ coloured by vorticity in the outlet section (instantaneous at $t = 2.25$ ms under hot (flame) conditions).*
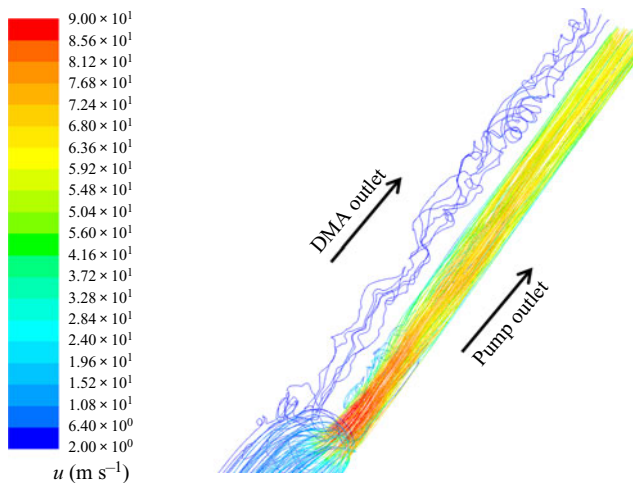

Figure 8. *Trajectories in the outlets coloured by velocity magnitude (instantaneous at $t = 2.25$ ms under hot (flame) conditions).*

numbers is a well known phenomenon as described and reviewed by Tsukahara, Seki, Kawamura, & Tochio (2005).

A more instructive result is obtained, when the isosurface is coloured by the mean mass fraction $\langle y_{CO_2} \rangle$ of CO_2, as shown in figures 9 and 10. According to figure 8, a ring type puff is observed approx. 200 mm (≈ 10 ms) downstream of the orifice. Obviously, the sampled flame gas disperses quite well in the hot boundary layer at the wall, but it does not mix into the interior of the dilution gas flow due to the large viscosity difference, as mentioned in § 2.2. Downstream of the puff (right-hand part of figure 9), the sampled gas is seen to creep along the hot boundary layer, but it fills only a small part of the total circumference. Figure 10 shows the mean mass fraction of CO_2 in the outlet section. The end plate of the dilution tube acts as an obstacle which causes high turbulence, as expected from figure 2. The mixing here is much better than in the preceding part of the dilution tube, but it is not complete, hence there remains a concentration difference of approximately 20 % in the two outlets. The creeping sample gas flow and the final concentration differences are also seen well in the RANS calculations (figure 11).
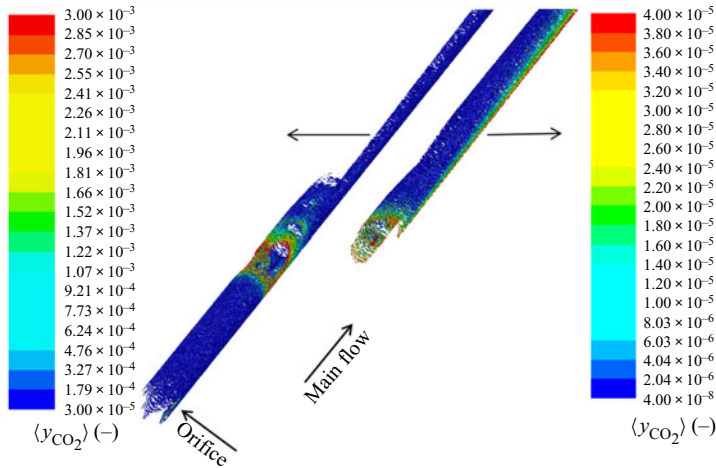
Figure 9. *Isosurface $Q = 4 \times 10^4\ s^{-2}$ coloured by mean mass fraction of CO_2 in the inlet section (left) and in the middle section (right) of the dilution tube (instantaneous at $t = 2.25$ ms under hot (flame) conditions).*
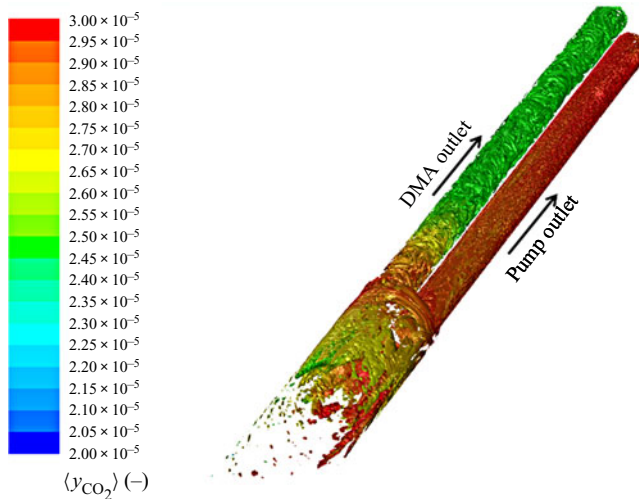

Figure 10. *Isosurface $Q = 4 \times 10^4\ s^{-2}$ coloured by mean mass fraction of CO_2 in the outlet section (instantaneous at $t = 2.25$ ms under hot (flame) conditions).*

4.3. Orifice flow rate and DR

Figure 12(*a*) shows the calculated orifice flow rates for ambient air and hot flame gas. The corresponding discharge coefficients are $C_{d,calc} = Q_{orf,calc}/Q_{orf,theoretical}$, where $Q_{orf,theoretical}$ is given by (1), setting $C_d = 1.0$. As shown in figure 12(*b*), for ambient air, the calculated discharge coefficient increases with increasing pressure drop, passes a maximum and drops farther on. This behaviour is in agreement with Berger et al. (2019). For the hot flame gas, surprisingly, the calculated discharge coefficient is only around 0.35, probably because of the increased viscosity and, it appears that the discharge coefficient scales with $\eta^{-1.75}$ (broken lines in figure 12*b*). Together with our previous reports (Mätzing & Stapf, 2019; Mätzing, Vlavakis, Trimis, & Stapf, 2022), the present study seems to be the first attempt to
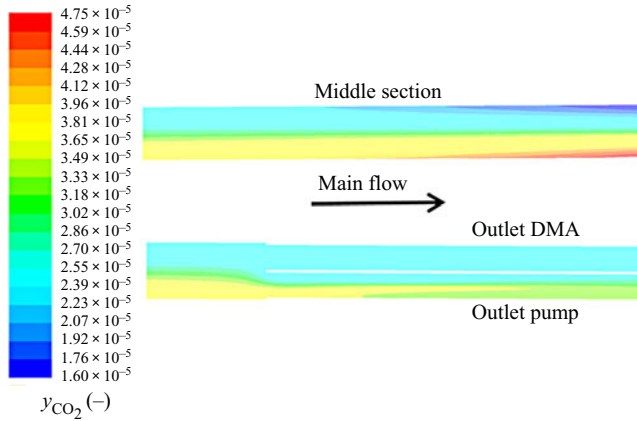
Figure 11. *Mass fraction of CO_2 in the middle section and in the outlet section of the dilution tube (RANS).*
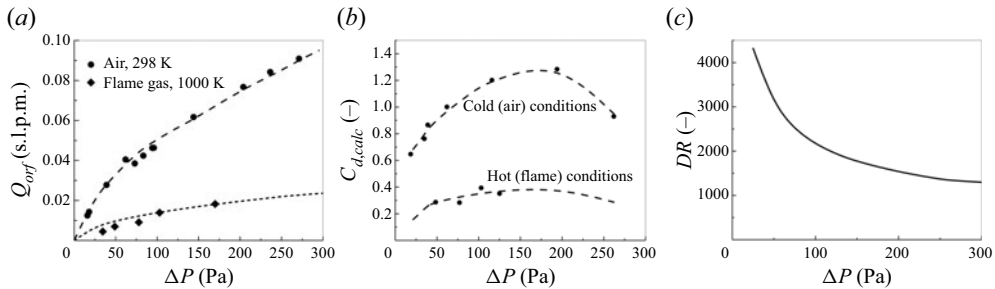

Figure 12. *(a) Calculated orifice flow: see (6). (b) Calculated discharge coefficients, broken lines: fit for cold (air) conditions and, fit using $C_d \propto \eta^{-1.75}$ for hot (flame) conditions. (c) The DR at the DMA outlet under flame conditions.*

investigate the orifice flow at high temperature by CFD and, no comparable investigation was found in the literature.

Figure 12(*c*) shows the DR for flame conditions which is calculated from figure 12(*a*) assuming homogeneous mixing (see comment in the discussion section). At the DMA outlet, $DR = 2160$ at $\Delta P = 100$ Pa and orifice diameter $D_{orf} = 0.3$ mm. Zhao, Yang, Wang, et al. (2003) reported $DR = 2 \times 10^4$ at $\Delta P = 100$ Pa for an orifice diameter of 0.2 mm. If the reported DR is normalized to $D_{orf} = 0.3$ mm via the ratio of orifice cross-sections, it drops to 8900, which is still much higher than calculated here. Similarly, if the present data are extrapolated to the conditions of Camacho et al. (2015) and Abid et al. (2008), wherein $D_{orf} = 0.127$ mm, $\Delta P = 980$ Pa, a DR of 130 is obtained, well below the reported DR, which are 450 and 620, respectively.

4.4. Embedded dilution tubes

As mentioned in the introduction, many studies of the soot formation zone employ cooled stagnation plates for flame stabilization which have embedded dilution tubes. The major difference to free-standing tubes is the much more intense cooling of the postflame gas and the tube wall down to temperatures as low as 400 K. Under these conditions, the cross-sectional gradients of viscosity and Reynolds number are smaller than in free-standing dilution tubes, which should favour the mixing process. On the other
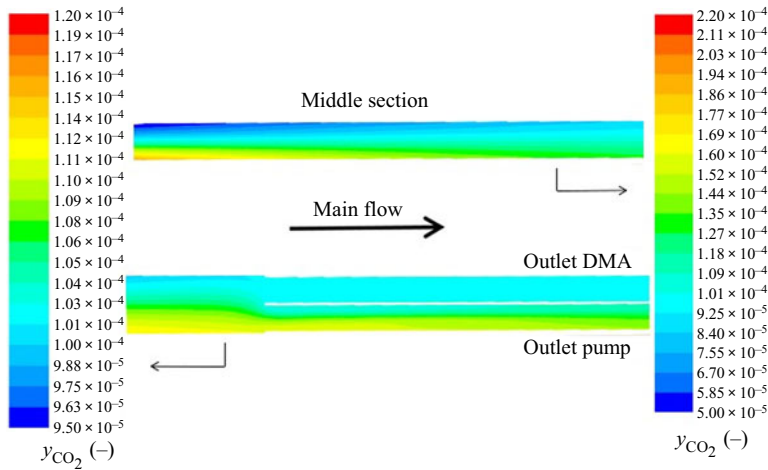
Figure 13. *Embedded dilution tube: mass fraction of CO_2 in the middle section and in the outlet section of the dilution tube (RANS).*

hand, the diffusion coefficient ($\propto T^{3/2}$) is reduced by a factor of 3.75 which is disadvantageous for the mixing process under low turbulence conditions.

Figure 13 shows the calculated concentration profiles, y_{CO_2}, in the middle and in the outlet sections. Due to the smaller temperature difference between the inert dilution gas and the sampled gas (as well as the wall temperature), the mixing process improves somewhat and, the calculated concentration difference at the DMA and pump outlets is only 5 %. The DR, however, is only $DR = 412$ for a pressure drop of $\Delta P = 100$ Pa, which is well below usual reports of experimental studies (Abid et al., 2008; Camacho et al., 2015; Tang et al., 2016).

5. Discussion

The gas flow and the mixing process in horizontal dilution tubes are difficult to investigate experimentally. Therefore, RANS calculations and LES were used here to test the important claims of the procedure, which are rapid mixing and quenching of the flame gas sample. The calculations were performed on two high resolution grids and grid independence was confirmed.

As first result, the *Re* number was found to decrease rapidly along the tube axis and the gas flow is shifted from the initial turbulent into the transitional flow regime. In terms of macroscopic gas properties, this is due to increasing gas temperature and to the associated increase of gas viscosity. On the microscale, it is due a specific turbulent dissipation rate around 4000 s^{-1} which translates into a relaxation time ~250 µs and a relaxation length scale ~4 mm only. Consequently, at the orifice location, the radial velocity profile is neither flat (as in turbulent conditions) nor is it parabolic (as in laminar case), which indicates transitional flow.

Farther downstream, significant turbulent structures develop close to the end plate of the dilution tube, where the gas flow is split into two outlet pipes with smaller diameters than in the main body of the dilution tube. In the pump outlet, the *Re* number is $>2 \times 10^4$ and the gas flow is clearly turbulent. In the DMA outlet, which carries only approximately 5 % of the total gas flow, the *Re* number is low (~800), but the trajectories are not straight and in parallel, as in laminar flow. Instead, they appear meandering, oscillating between different locations of the wall. This means that turbulent structures persist in the DMA outlet. Moreover, this situation is disadvantageous for undisturbed, reliable and reproducible gas and particle sampling.

The gas flow through the sampling orifice was interpreted in terms of a jet in cross-flow configuration. Under ambient air conditions, which correspond to the calibration procedure in experimental studies,

the discharge coefficient at the orifice was found to be in the range 0.6–1.2 and to pass a maximum at a pressure drop $\Delta P \approx 150$ Pa, in agreement with previous literature data (Berger et al., 2019). Under the hot (1000 K) conditions met in free-standing dilution tubes, the discharge coefficient dropped to values below 0.4. This is probably due to increased viscosity, and a correlation $C_d \propto \eta^{-1.75}$ appears to explain the results.

Based on these results, the DR was determined assuming homogeneous dilution in the inert gas flow. In agreement with experimental results, the DR was found to decrease almost exponentially with increasing pressure drop. However, the experimental DR often depend on some assumption about the nature of the orifice flow and the accuracy is limited roughly to a factor of three (Abid et al., 2008; Camacho et al., 2015). In addition, experimental DR have a tendency to turn out too high because of eventual clogging which decreases the orifice size. The uncertainties associated with clogging are also approximately a factor of three in DR (Abid et al., 2008). As shown above, the DR calculated here are significantly smaller than those given in literature reports, both for free-standing and for embedded dilution tubes. They are approximately a factor of five below reported averages and fall below the reported lower limits.

Most importantly, for both free-standing and embedded dilution tubes, the mixing process was found to be incomplete at the available time scale. Therefore, significant concentration gradients persist and do not cancel out in the outlets. In case of the much hotter gas samples of free-standing dilution tubes, this effect is more pronounced than in the intensively cooled embedded dilution tubes. This also means that DR which are based on the assumption of complete, homogeneous mixing can only be regarded as rough estimates. A separate test calculation was performed with much higher dilution gas flow, in a way that the Reynolds number increased to 2×10^4 in the main body of the dilution tube. But even then, the mixing process was still incomplete in the outlet section. A more careful experimental testing of the performance of horizontal dilution tubes is recommended, e.g. using test gas samples and test aerosol particles of known size distribution.

To improve the performance of horizontal dilution tubes, it appears that the jet-to-cross-flow momentum flux ratio should be increased, either by applying a higher pressure drop at the orifice or by reducing the dilution gas flow rate. In addition, small obstacles might be installed in the tube upstream of the orifice, in order to increase the turbulence intensity in a similar way as it is now occurring at the tube outlets. Also, a dilution gas of low viscosity and/or high diffusivity may improve the mixing process.

6. Conclusions

Horizontal dilution tubes are widely used for flame gas and particle sampling. The present CFD analysis focuses on the cooling and mixing processes inside the dilution tubes. Grid independence and validity of RANS results were confirmed. Therefore, while LES helps us to understand the flow properties on the microscale, RANS calculations have proved to be reliable tools for the assessment of the overall performance of horizontal dilution tubes. A major advantage of the CFD approach is to calculate DR without particular assumptions about the nature of the orifice flow. The results show that the turbulence of the dilution gas flow and the jet to cross-flow momentum flux ratio are too low to ensure high mixing and quenching rates at the time scales available.

Experimental set-ups may differ from the case which is studied here. In a similar previous study (Mätzing & Stapf, 2019), the tube diameter was a factor of two smaller, the material was stainless steel and the outlets were perpendicular to each other. The major results, however, were quite comparable to those reported here. Therefore, differences in absolute dimensions, tube materials and configuration are expected to be of minor importance. While the reported experimental DR have uncertainties around a factor of three, the DR were calculated here to be roughly a factor of five below reported averages. But also, the mixing process was found to be incomplete. Therefore, the concept of a well-defined DR appears questionable and, the experimental procedure needs improvement.

This study has also shown that there are only limited literature data available about high-temperature orifice flows.

Future studies, both experimental and theoretical, should be undertaken to optimize the performance of horizontal dilution tubes in terms of accurate and reliable sampling. According to the jet in cross-flow concept, this can be achieved by proper adjustment of the gas flow rates. The major drawback is the low turbulence in the vicinity of the sampling orifice. It may be increased by a more appropriate design of the dilution tubes. In addition, the installation of flow resistors may help to increase the turbulence of the dilution gas flow.

References

Abid, A.D., Heinz, N., Tolmachoff, E.D., Phares, D.J., Campbell, C.S., & Wang, H. (2008). On evolution of particle size distribution functions of incipient soot in premixed ethylene–oxygen–argon flames. *Combustion and Flame*, *154*, 775–788.

Adamson, B.D., Skeen, S.A., Ahmed, M., & Hansen, N. (2018). Detection of aliphatically bridged multi-core polycyclic aromatic hydrocarbons in sooting flames with atmospheric-sampling high-resolution tandem mass spectrometry. *Journal of Physical Chemistry A*, *122*, 9338–9349.

Appel, J., Bockhorn, H., & Frenklach, M. (2000). Kinetic modelling of soot formation with detailed chemistry and physics. *Combustion and Flame*, *121*, 122–136.

Berger, S., Gourdain, N., Bauerheim, M., & Devillez, S. (2019). Discharge coefficient of an orifice jet in crossflow: Influence of inlet conditions and optimum velocity ratio. *AIAA Aviation 2019 Forum, Dallas*, *June 2019*. Retrieved from https://hal.archives-ouvertes.fr/hal-02166754

Borutzky, W., Barnard, B., & Thoma, J. (2002). An orifice flow model for laminar and turbulent conditions. *Simulation Modelling Practice and Theory*, *10*, 141–152.

Camacho, J., Liu, C., Gu, C., Lin, H., Huang, Z., Tang, Q., . . . Wang, H. (2015). Mobility size and mass of nascent soot particles in a benchmark premixed ethylene flame. *Combustion and Flame*, *162*, 3810–3822.

Chang, J., Shao, X., Hu, X., & Zhang, S. (2016). Flow characteristics of a low Reynolds number jet in crossflow with an obstacle block. *The Open Fuels & Energy Science Journal*, *9*, 1876–973X/16.

Commodo, M., Sgro, L.A., Minutolo, P., & D'Anna, A. (2013). Characterization of combustion-generated carbonaceous nanoparticles by size-dependent ultraviolet laser photoionization. *Journal of Physical Chemistry A 2013, 117*, 3980–3989.

Commodo, M., De Falco, G., Bruno, A., Borriello, C., Minutolo, P., & D'Anna, A. (2015). Physicochemical evolution of nascent soot particles in a laminar premixed flame: From nucleation to early growth. *Combustion and Flame*, *162*, 3854–3863.

Corson, J., Mulholland, G.W., & Zachariah, M.R. (2018). Hydrodynamic interactions between aerosol particles in the transition regime. *Journal of Fluid Mechanics*, *855*, 535–553.

Egolfopoulos, F.N., Hansen, N., Ju, Y., Kohse-Höinghaus, K., Law, C., & Qi, F. (2014). Advances and challenges in laminar flame experiments and implications for combustion chemistry. *Progress in Energy and Combustion Science*, *43*, 36–67.

Frenklach, M., & Mebel, A.M. (2020). On the mechanism of soot nucleation. *Physical Chemistry Chemical Physics*, *22*, 5314–5331.

Frenzel, I., Krause, H., & Trimis, D. (2017). Study on the influence of ethanol and butanol addition on soot formation in iso-octane flames. *Energy Procedia*, *120*, 721–728.

Friedlander, S.K. (2000). *Smoke, dust and haze*. Oxford, UK: Oxford University Press.

Fröhlich, J. (2006). *Large eddy simulation turbulenter Strömungen*. Wiesbaden, Germany: Teubner.

Gerasimov, A. (2016). Quick guide to setting up LES-type simulations, Version 1.4. Retrieved from http://www.tfd.chalmers.se/~lada/comp_turb_model/postscript_files/Quick_Guide_to_Setting_Up_LES_version_1.4_for_Lars.pdf

Ghiassi, H., Jaramillo, H.C., Toth, P., & Lighty, J.S. (2016). Soot oxidation-induced fragmentation: Part 2: Experimental investigation of the mechanism of fragmentation. *Combustion and Flame*, *163*, 170–178.

Gururajan, V., Egolfopoulos, F.N., & Kohse-Höinghaus, K. (2015). Direct numerical simulation of probe effects in low-pressure flame sampling. *Proceedings of the Combustion Institute*, *35*, 821–829.

Hansen, N., Cool, T.A., Westmoreland, P.R., & Kohse-Höinghaus, K. (2009). Recent contributions of flame-sampling molecular-beam mass spectrometry to a fundamental understanding of combustion chemistry. *Progress in Energy and Combustion Science*, *35*, 168–191.

Haynes, B.S., & Wagner, H.G. (1981). Soot formation. *Progress in Energy and Combustion Science*, *7*, 229–273.

Holmén, V. (2012). *Methods for vortex identification* (MA thesis). Retrieved from https://lup.lub.lu.se/student-papers/search/publication/3241710

Jiang, M., Machiraju, R., & Thomson, D. (2005). Detection and visualization of vortices. In C. Johnson & C. Hansen (Eds.), *Visualization handbook* (pp. 295–309). Burlington, MA: Elsevier.

Johansson, K.O., Head-Gordon, M.P., Schrader, P.E., Wilson, K.R., & Michelsen, H.A. (2018). Resonance-stabilized hydrocarbon-radical chain reactions may explain soot inception and growth. *Science*, *361*, 997–1000.

Karagozian, A.R. (2014). The jet in crossflow. *Physics of Fluids*, *26*, 101303.

Kasper, M., Siegmann, K., & Sattler, K. (1997). Evaluation of an in situ sampling probe for its accuracy in determining particle size distributions from flames. *Journal of Aerosol Science*, *28*, 1569–1578.

Köhler, M., Oßwald, P., Xu, H., Kathrotia, T., Hasse, C., & Riedel, U. (2016). Speciation data for fuel-rich methane oxy-combustion and reforming under prototypical partial oxidation conditions. *Chemical Engineering Science*, *139*, 249–260.

Kolár, V. (2011). Brief notes on vortex identification. In A. Zemliak & N. Mastorakis (Eds.), *Proceedings 8th WSEAS International Conference on Fluid Mechanics, World Scientific and Engineering Academy and Society (WSEAS), Stevens Point, WI, USA* (pp. 23–28).

Lafferty, J.M. (Ed.). (1998). *Foundations of vacuum science and technology*. New York, NY: Wiley.

Mahesh, K. (2013). The interactions of jets with crossflow. *Annual Review of Fluid Mechanics*, *45*, 379–407.

Mätzing, H., & Stapf, D. (2019). Modelling soot particle inception and soot particle probe sampling. Retrieved from https://doi.org/10.5445/IR/1000094019

Mätzing, H., Vlavakis, P., Trimis, D., & Stapf, D. (2022). A CFD study of the performance of horizontal dilution tubes. In *13th European Conference on Industrial Furnaces and Boilers (INFUB-13), Algarve, Portugal, April 19–22*. Retrieved from https://infub.pt/abstractpaperbackup.axd?id=591&key=00043E9968

Muppidi, S., & Mahesh, K. (2005). Study of trajectories of jets in crossflow using direct numerical simulations. *Journal of Fluid Mechanics*, *530*, 81–100.

Oertel, H., Prandtl, L., & Böhle, M. (2008). *Prandtl – Führer durch die Strömungslehre*. Wiesbaden, Germany: Vieweg + Teubner.

Saggese, C., Cuoci, A., Frassoldati, A., Ferrario, S., Camacho, J., Wang, H., & Faravelli, T. (2016). Probe effects in soot sampling from a burner-stabilized stagnation flame. *Combustion and Flame*, *167*, 184–197.

Sgro, L.A., Barone, A.C., Commodo, M., D'Alessio, A., De Filippo, A., Lanzuolo, G., & Minutolo, P. (2009). Measurement of nanoparticles of organic carbon in non-sooting flame conditions. *Proceedings of the Combustion Institute*, *32*, 689–696.

Skovorodko, P., Tereshchenko, A., Korobeinichev, O., Knyazkov, D., & Shmakov, A.G. (2013). Experimental and numerical study of probe-induced perturbations of the flame structure. *Combustion Theory and Modelling*, *17*, 1–24.

Stelzner, B., Weis, C., Habisreuther, P., Zarzalis, N., & Trimis, D. (2017). Super-adiabatic flame temperatures in premixed methane flames: A comparison between oxy-fuel and conventional air combustion. *Fuel*, *201*, 148–155.

Struckmeier, U., Oßwald, P., Kasper, T., Böhling, L., Heuser, M., Köhler, M., . . . Kohse-Höinghaus, K. (2009). Sampling probe influences on temperature and species concentrations in molecular beam mass spectroscopic investigations of flat premixed low-pressure flames. *Zeitschrift für Physikalische Chemie*, *223*, 503–537.

Tang, Q., Mei, J., & You, X. (2016). Effects of CO_2 addition on the evolution of particle size distribution functions in premixed ethylene flame. *Combustion and Flame*, *165*, 424–432.

Tsukahara, T., Seki, Y., Kawamura, H., & Tochio, D. (2005). *DNS of turbulent channel flow at very low Reynolds numbers*. 4th International Symposium on Turbulence and Shear Flow Phenomena (pp. 935–952). Clear Spring, MD: Dorley House Books.

Wagner, H.G. (1979). Soot formation in combustion. *Symposium (International) on Combustion*, *17*, 3–19.

Wang, H. (2011). Formation of nascent soot and other condensed-phase materials in flames. *Proceedings of the Combustion Institute*, *33*, 41–67.

Zhao, B., Yang, Z., Johnston, M.V., Wang, H., Wexler, A.S., Balthasar, M., & Kraft, M. (2003). Measurement and numerical simulation of soot particle size distribution functions in a laminar premixed ethylene-oxygen-argon flame. *Combustion and Flame*, *133*, 173–188.

Zhao, B., Yang, Z., Wang, J., Johnston, M.V., & Wang, H. (2003). Analysis of soot nanoparticles in a laminar premixed ethylene flame by scanning mobility particle sizer. *Aerosol Science and Technology*, *37*, 611–620.

Zirwes, T., Häber, T., Zhang, F., Kosaka, H., Dreizler, A., Steinhausen, M., . . . Bockhorn, H. (2021). Numerical study of quenching distances for sidewall quenching using detailed diffusion and chemistry. *Flow, Turbulence and Combustion*, *106*, 649–679. Retrieved from https://doi.org/10.1007/s10494-020-00215-0